

# Image-Based Models of Cardiac Structure with Applications in Arrhythmia and Defibrillation Studies\*

Fijoy Vadakkumpadan, Lukas J Rantner, Brock Tice, Patrick Boyle, Anton J Prassl, Edward Vigmond, Gernot Plank<sup>§</sup>, Natalia Trayanova.

\*Short title: Image-Based Cardiac Models with Applications

<sup>§</sup>Corresponding author: G. Plank, PhD

Institute of Biophysics and Institute of Physiology,  
Medical University of Graz,  
Harrachgasse 21/IV, A-8010 Graz, Austria  
Tel.: (++43) (316) 380 7745; Fax: (++43) (316) 380 9660  
Email: [gernot.plank@meduni-graz.at](mailto:gernot.plank@meduni-graz.at)

F. Vadakkumpadan, PhD, L. J. Rantner, MS, B. Tice, BS, and N. Trayanova, PhD, are with the Institute for Computational Medicine and the Department of Biomedical Engineering, Johns Hopkins University, MD, USA

A. J. Prassl is with the Institute of Biophysics, Medical University of Graz, Graz, Austria

P. Boyle, BS, and E. Vigmond, PhD, are with the Department of Electrical and Computer Engineering, University of Calgary, AB, Canada

This work was supported by NIH grants R01-HL063195, R01-HL082729 and R01-HL067322, and the NSF grant CBET-0601935 to NT.

## ABSTRACT

The objective of this article is to present a set of methods for constructing realistic computational models of cardiac structure from high resolution structural and diffusion tensor (DT) magnetic resonance (MR) images, and to demonstrate the applicability of the models in simulation studies. The structural image is segmented to identify various regions such as normal myocardium, ventricles, and infarct. A finite element mesh is generated from the processed structural data, and fiber orientations are assigned to the elements. The Purkinje system, when visible, is modeled using linear elements that interconnect a set of manually identified points. The methods were applied to construct two different models, and two simulation studies, which demonstrate the applicability of the models in the analysis of arrhythmia and defibrillation, were performed. The models represent cardiac structure with unprecedented detail for simulation studies.

## I. INTRODUCTION

THE primary cumulative goal of all cardiac research is a comprehensive understanding of the structure and function of the heart in health and disease. A key to achieving this goal is the integration of information obtained at various levels, from ion channels and calcium cycling to activation maps and regional strain distributions. Computational modeling provides a powerful tool to address this challenge and is thus becoming essential for the complete understanding of the heart. Computational approaches require finite element representations (or models) of the geometry and fiber architecture of the cardiac tissue (1). The cardiac architecture must be accurately acquired in order to construct realistic models. Recent advances in magnetic resonance (MR) imaging technologies have facilitated the acquisition of geometry and tissue architecture of the heart at very high spatial resolution. Modern anatomical MR scanners can image the cardiac histo-anatomy of small experimental animals, such as rabbit, with an isotropic resolution in the order of  $10^{-5}$  m (2). Advanced diffusion tensor (DT) MR equipments can measure the diffusivity of water in the tissue with a resolution in the order of  $10^{-4}$  m (3). The primary eigenvectors of the diffusion tensors have been shown to be aligned with the prevailing cardiomyocyte orientations, commonly referred to as “fiber orientations”. Evidence also suggests that the secondary and tertiary eigenvectors are oriented normally to the main cell axes, in the myocardial laminar plane and perpendicular to it, respectively.

The objective of this article is twofold. First, we present a set of generic methods which we have developed for constructing detailed computational models of the heart from high resolution structural and diffusion tensor (DT) magnetic resonance (MR) images. Second, we demonstrate the application of these models in the study of arrhythmia and defibrillation. The models that we present contain unprecedented structural detail, opening enhanced opportunities for modeling cardiac function. In the following, Section II presents the methods for generating whole-heart models, Section III presents the reconstructed whole-heart models, Section IV describes the reconstruction of the Purkinje network, Section V reports results of

electrophysiological simulation studies, demonstrating the utility of image-based modeling in arrhythmia and defibrillation research, and Section VI concludes the paper.

## II. METHODOLOGY FOR IMAGE-BASED WHOLE-HEART MODEL GENERATION

### *A. Segmentation of the Structural Image*

To generate image-based models of the heart, it is necessary to classify (or segment) the voxels in the structural MR image into different groups, such as normal tissue, diseased tissue (or infarct), background, etc. Segmentation of high-resolution cardiac images is a very challenging task because of the complex geometry and topology of the myocardium, measurement noise, blurred object boundaries in the images, and the overlap of image intensities between different voxel groups. After extensive experimentation with various existing segmentation techniques such as edge detection, deformable models, region growing, level set methods, k-means clustering etc. (4), we developed a processing pipeline for the segmentation of the structural MR image as illustrated in Figure 1. The figure shows the results as an example image slice is processed through the steps 1 to 4 in the pipeline. Step 1 in the figure shows the original example slice. The steps of the pipeline are explained in detail below.

#### *1) Suspension medium removal*

In the first step of our segmentation pipeline, the structural MR image is processed to label and "remove" the voxels corresponding to the cavity content, and the medium in which the heart was suspended during the image acquisition. A combination of edge detection, region growing, and manual editing is used in this step. The edge detection is performed in each slice of the image, by first computing the intensity variance of the two-dimensional (2D) local neighborhood of each voxel in the slice, and then by selecting voxels with a variance above a certain threshold. Step 1 in Figure 1 shows the edges for the example slice. The collection of image slices after the edge detection forms the edge image, a three dimensional (3D) map of the 2D edges.

From the edge image, the myocardial boundary of the whole heart is extracted using a 3D region growing algorithm. This algorithm, when initialized with a user defined voxel, identifies a voxel set such that the set forms a connected structure, which includes the user defined voxel; the members of the set have the same image intensity. Next, from the image that represents the myocardial boundary, voxels that correspond to the suspension and cavity medium are extracted using the region growing algorithm. Finally, the suspension medium is removed from the original structural MR image by assigning the background intensity to all voxels that correspond to the medium. Step 1 in Figure 1 shows the myocardial boundary, suspension medium, and myocardium for the example slice. The collection of image slices after the removal of the suspension medium forms a 3D image of the myocardium.

## 2) *Level set segmentation*

In the next step, a level set method is applied to the image of the myocardium, to separate the larger coronary arteries and interlaminar clefts, as well as to refine the myocardial boundary extracted during the previous steps. Level set methods have the inherent capability to implicitly track complex topologies. This characteristic makes them highly suitable for the delineation of the complex coronary artery network and interlaminar clefts. In the level set methods, the segmentation is achieved through the evolution of a surface  $\Gamma$ , which is implicitly represented as the zero level set of a time-dependent 3D function  $\Phi(x, y, z, t)$ , i.e.  $\Gamma(t) = \{x, y, z \mid \Phi(x, y, z, t) = 0\}$ , where  $x, y, z$  are the Cartesian coordinates, and  $t$  is the time. The evolution of  $\Phi$  is formulated as a partial differential equation, which contains terms for advancing the surface based on image intensities, smoothing the surface, and attracting the surface to the edges in the image. For detailed information on the level set segmentation, the reader is referred to (5). Step 2 in Figure 1 illustrates the level set segmentation for the example slice. It must be noted that it is necessary to remove the suspension medium before the level set segmentation, because the surface may

otherwise evolve into the medium in image regions where the boundary between myocardium and medium is blurred.

### 3) *Segmentation of ventricles*

In the third step of our model generation pipeline, segmentation of the ventricular myocardium is performed in order to account for the presence of an insulating layer of connective tissue between the atria and the ventricles (annulus fibrosus), as well as to assign different electrophysiological properties (atrial vs. ventricular) to the tissue on either side of this boundary. To perform this step, in each slice, the ventricular portion of the tissue is labeled by fitting a closed spline curve through landmark points placed around the ventricles and along the atrio-ventricular (AV) border. All voxels that belong to tissue inside the curve are marked as ventricular. Step 3 in Figure 1 shows the landmarks, spline, and ventricular myocardium for the example slice. The identification of landmark points is performed manually for a number of slices that are evenly distributed in the image. The manual placement of the landmarks is guided by the elevated voxel intensity of the dense tissue along the AV border, and the location of AV valves. The landmarks for the remaining slices are obtained by linearly interpolating the manually identified points.

Mathematically, let  $s_1, s_2, s_3, \dots, s_n$  denote the sequence of slices in the image, and let  $s_{i_1}, s_{i_2}, s_{i_3}, \dots, s_{i_m}$  denote the slices for which the landmarks are identified manually, where  $i_1 < i_2 < i_3 < \dots < i_m$ . The number of landmarks is the same in every slice. Let  $p$  denote the number of landmarks, and let  $l_1, l_2, l_3, \dots, l_p$  denote the landmarks. Note that a landmark in one slice is denoted by the same index as the corresponding landmark in any other slice. If  $(x_j^{i_a}, y_j^{i_a})$  and  $(x_j^{i_{a+1}}, y_j^{i_{a+1}})$  are the coordinate pairs of landmark  $l_j$  on slices  $s_{i_a}$  and  $s_{i_{a+1}}$  respectively, then the coordinates of  $l_j$  on slices  $s_k$ ,  $i_a < k < i_{a+1}$  are given by

$$\begin{cases} x_j^k = x_j^{i_a} + \frac{(j-i_a)}{(i_{a+1}-i_a)}(x_j^{i_{a+1}} - x_j^{i_a}), \\ y_j^k = y_j^{i_a} + \frac{(j-i_a)}{(i_{a+1}-i_a)}(y_j^{i_{a+1}} - y_j^{i_a}) \end{cases} \quad (1)$$

#### 4) *Infarct segmentation*

After the delineation of the ventricles, any infarct tissue present is labeled using a combination of level set segmentation of the fractional anisotropy (FA) image, intensity thresholding of the anatomical image. In this procedure, the DTMR image is interpolated to the resolution of the structural MR image, if the resolution of the latter is higher. The interpolation of the DTMR image is performed by first linearly interpolating the diffusion-weighted images to the desired resolution, and then recalculating the local diffusion tensors using existing methods (6). From the interpolated DTMR image, the FA image is generated by computing the FA of the diffusion tensor at each voxel (7). The FA is a measure of the directional diffusivity of water, and its values range from 0 to 1. A value of 0 indicates perfectly isotropic diffusion, and 1 indicates perfectly anisotropic diffusion. The infarct region is characterized by lower anisotropy, and therefore lower FA values, compared to the healthy myocardium (8), because of the myocardial disorganization in the infarct. Based on this difference in FA values, the infarct region is separated from the normal myocardium by applying a level set segmentation to the 3D FA image. Step 4 in Figure 1 shows the segmentation of the FA image slice which corresponds to the example slice. Next, the infarct region is subdivided into two areas, a core, which is assumed to contain inexcitable scar tissue, and a border zone, which is assumed to contain excitable but pathologically remodeled tissue, by thresholding the structural MR image based on the intensity values of the voxels. The core has high or low intensity, while the border zone has medium intensity (9, 10). Step 4 in Figure 1 illustrates the final segmentation of the example slice. Once any infarct areas present are identified, segmentation of the structural MR image is complete.

### *B. Mesh generation*

Next, a finite element mesh is generated from the segmented structural MR image using Tarantula, a commercial software (<http://www.meshing.at/Spiderhome/Tarantula.html>). Details regarding the mesh generation methodology can be found in a recent paper (11). The software is very robust, produces boundary-fitted, locally-refined, smooth conformal meshes, and allows the user to select the desired resolution in various regions. The software automatically assigns region identifiers to the elements based on the segmentation, thereby differentiating the elements that belong to the infarct regions, the ventricles, or the rest of the tissue. Figure 2a shows a mesh generated for the segmented slice shown in Figure 1. Figure 2b presents a small region of the mesh in detail. As the figure illustrates, the interior tissue volume is meshed at low resolution, while the interface between tissue and non-tissue is refined by a factor of about two. This local adaptation of the resolution significantly reduces the number of elements in the mesh without compromising the geometric detail.

### *C. Fiber mapping*

In the final step of the model generation pipeline, fiber orientations are mapped onto the anatomical mesh by interpolating the primary diffusion vectors on the centroids of the elements. First, a reference vector field is constructed by computing the primary eigenvector of each tensor in the previously interpolated DTMR image. This vector field is in the same coordinate system as the finite element mesh. The fiber orientation assigned to an element in the mesh is the direction of that vector in the reference field nearest to the centroid of the element. Figure 3a shows the derived fiber orientations, mapped to the mesh shown in Figure 2a. Figure 3b shows a small region in more detail.

## III. DATASETS AND WHOLE-HEART MODELS

Models were generated from MR datasets of a normal rabbit heart and a rabbit heart with cardiac infarction. For the infarcted heart, both structural MR and DTMR images were acquired, at resolutions of  $61 \times 61 \times 60 \mu\text{m}^3$  and  $122 \times 122 \times 500 \mu\text{m}^3$  respectively. The infarct was four weeks old and induced by

occlusion of the lateral division of the coronary artery (12). For the normal heart, only the structural MR image was acquired, at a very high resolution of  $26.5 \times 26.5 \times 24.5 \mu\text{m}^3$ . These datasets have been used in a previous studies, where data acquisition techniques have been described (2, 13).

Models were generated from the previously described high-resolution 3D cardiac images of normal and infarcted rabbits. Figure 4 visualizes the generated whole-heart models. In each row, the first column shows the anterior view of the entire organ model, and the second and third columns show the model split open along the horizontal long axis view plane. Ventricles, infarct cores, and border zones are shown in dark red, yellow, and blue, respectively. The developed methods have reconstructed the overall geometries of the hearts. In the normal rabbit heart dataset, the atria had collapsed in the process of data acquisition, which necessitated the removal of all tissue that does not belong to the ventricular myocardium. The normal rabbit model consisted of approximately 31 million elements, and the infarcted model consisted of 1 million elements. The average edge lengths in the normal and infarcted models were  $50 \mu\text{m}$  and  $230 \mu\text{m}$  respectively.

Figure 5a shows an enlarged view of the muscular trabeculations in the basal region of the right ventricular chamber in the normal rabbit model. Figure 5b presents a papillary muscle that is attached to the mitral valve in the infarcted rabbit model. Figure 5c shows the extracted coronary vessels and interlaminar clefts in the normal rabbit model. Note that the vessels and clefts are separated from the rest of the myocardium during the level set segmentation. The reconstruction of the papillary muscles and of the complex network of trabeculations, arteries, and interlaminar clefts illustrate the high resolution of the structural detail that can be obtained using the methods developed here.

Visualization of the 3D arrangement of fiber orientations in the heart is a challenging problem. A common solution is to use the so-called streamlining method (14). In this method, fiber orientation is displayed as a track, which is traced by moving a particle according to the velocity field defined by the

primary diffusion vectors. To obtain a smooth visualization, it is important to remove measurement noise by filtering the velocity field. To do so, we used a locally regularizing filter called the Perona-Malik Nonlinear Anisotropic filter (15). Figure 6 displays the primary eigenvector tracks for the infarcted rabbit model. A visual comparison of the tracks with existing anatomical data (16, 17) verifies the qualitative correlation of the fiber orientations in these models.

#### IV. PURKINJE SYSTEM MODELING

We have developed a methodology for reconstructing the Purkinje System (PS) from a high-resolution structural MR image and a finite element mesh representing the normal rabbit ventricles. Explicit reconstruction of the Purkinje system incorporates additional structural detail into the whole-heart model, and allows the user to assign distinct electrophysiological properties to the Purkinje system. For each slice in the image, branching points within the free-running PS (Purkinje-Purkinje Junctions, PPJ) and points where the PS entered the myocardium (Purkinje-Myocardial Junctions, PMJ) are identified by visual inspection and spatial coordinates these points are recorded. To construct the model of the free-running PS, the PMJ and PPJ points are mapped onto the closest vertices in the finite element mesh and connected using linear elements, with intermediate points or tags inserted in segments that deviated noticeably from straight lines. While this eliminated the elegant curvature of the physical system, the preservation of junctions and bifurcations ensures that the resulting model is an excellent approximation from an electrophysiological perspective.

The above methodology was applied to the high-resolution structural MR image of the normal rabbit heart and the corresponding finite element mesh. Figure 7 shows the results. Figure 7A shows a slab of the mesh that lies between two short axis planes. Figure 7B illustrates the PMJs, PPJs, and tags on a short axis slice of the image. The inset in Figure 7B displays the enlarged view of the small region enclosed in the red box. In the right ventricle (RV), there were 70 PPJs and 71 PMJs, with 49 of PMJs being found on the free wall, 10 on papillary muscles, and 12 on the septum. In the larger left ventricle (LV), 138 PPJs

and 99 PMJs were found, with 61, 24, and 14 PMJs respectively situated at the sites reported for the RV. Figure 7C shows the reconstructed model of the entire Purkinje system, and Figure 7D shows the Purkinje system overlaid on the mesh.

## V. SIMULATION EXAMPLES OF DEFIBRILLATION AND ARRHYTHMIA IN THE GENERATED MODELS

In this section, we present two different electrophysiological simulation examples using each of the two models presented in Section III. The first study uses the infarcted rabbit model to investigate the influence of the infarct core on the formation of virtual electrodes at defibrillation shock-end. In the second study, the right-ventricular free wall extracted from the high-resolution normal rabbit model is subject to pacing stimuli to examine re-entrant waves. These studies employ cardiac models with unprecedented structural detail, and demonstrate the utility of image-based modeling in arrhythmia and defibrillation research. The studies have not been published previously.

### A. Shock-end virtual electrode polarization in infarcted rabbit model

The infarcted rabbit model was used for a bidomain simulation study of virtual electrode polarization (VEP) formation at shock-end. We hypothesized that the infarct core would influence the formation of VEPs in the area of the core. Different VEP patterns at shock-end can ultimately lead to different post-shock propagating behavior and, in the case of defibrillation shocks, to different shock outcomes. For example, positive VEPs can lead to repolarization in regions where tissue is excitable (termed “make” excitation, as it occurs at shock onset). Negative VEP, on the other hand, can deexcite action potentials, creating post-shock excitable gaps. Close spatial proximity of such deexcited regions with positive VEPs can result in “break” excitation at shock-end (18).

The left ventricular shocks were defined to occur when a plate electrode next to the left ventricle (blue bar in Figure 8a and Figure 8b) was used as the cathode and a plate electrode next to the right ventricle (red bar in Figure 8a and Figure 8b) was used as ground. For right ventricular shocks, the opposite

arrangement was used. Left and right ventricular shocks of 1 and 5 V/cm strength and of 5 ms duration each were applied with a coupling interval (the time between the last pacing stimulus and shock onset) of 160 ms after apical pacing.

The Mahajan–Shiferaw rabbit ventricular ionic model was used to simulate the action potential (19). This ionic model is capable of representing the properties of fast ventricular action potential of the rabbit, and therefore it is a model well suited for the study of arrhythmia and arrhythmia therapy. In order to account for the behavior of ventricular myocytes after applied shocks (18, 20), and to maintain stability during the drastic changes in transmembrane potentials occurring during shocks (21), the ionic model was modified by adding electroporation and  $I_a$  current. It was assumed that  $I_a$  is part of the  $K^+$  flow through the L-type  $Ca^{2+}$  channel  $I_{Ca,L}$  (18). The infarct core was modeled as passive tissue with a resting potential of  $-80$  mV (22). The intracellular and extracellular longitudinal conductivities were both set to 0.295 S/m. The transverse conductivities were set to 0.046 S/m and 0.184 S/m for the intracellular and extracellular spaces respectively (23). For the infarct core, normal conductivity values were reduced by half (24).

Figure 8a shows the whole heart model in an anterior–posterior view (i.e., the heart is viewed from the front, the right ventricle can be seen on the left, the left ventricle can be seen on the right). The border zone is marked in green, and the infarct core is marked in blue. Figure 8b shows the posterior part of the heart after the model was cut in half along a coronal plane. Figure 8c through Figure 8f display the simulation results overlaid on the coronal cut. Figure 8c shows the distribution of transmembrane potential  $V_m$  at shock-end of a 1 V/cm left ventricular shock, Figure 8d shows  $V_m$  at shock-end of a 5 V/cm left ventricular shock, Figure 8e shows  $V_m$  at shock-end of a 1 V/cm right ventricular shock, and Figure 8f shows  $V_m$  at shock-end of a 5 V/cm right ventricular shock. Note that both the border zone was modeled as infarct core, resulting in a larger core, and no border zone. The region of the infarct core is approximately marked by the black squares in Figure 8c through Figure 8f. The color bar for

transmembrane potentials shown in the bottom panel applies to Figure 8c through Figure 8f.

The results show that, at shock-end, VEP is present in all transmural areas of the heart, with virtual cathodes facing the ground electrodes and virtual anodes facing the cathodes (plate electrodes). Also, with higher shock strengths, the gradients in transmembrane potential between virtual cathodes and anodes become steeper and virtual anodes and cathodes lie closer together spatially. In Figure 8c and Figure 8e (1 V/cm shocks), large areas of tissue lie between positive (red) and negative (blue) VEPs. In Figure 8d and Figure 8f (5 V/cm shocks), on the other hand, positive and negative VEPs lie closer together. Close to the site of the infarction (see Figure 8b), the virtual anode (blue color coding) is more pronounced than in other parts of the tissue. For 1 V/cm shocks (Figure 8c and Figure 8e), no virtual cathode (red color coding) is present in the area of the infarction.

This more prevalent virtual anode, in conjunction with a less prevalent virtual cathode, leads to an increased excitable gap in the area of the infarction. Defibrillation shocks are successful if they abolish fibrillatory activity and do not induce new fibrillation wavefronts. In terms of VEPs, defibrillation shocks are successful if make and break excitations travel through shock-induced excitable gaps before the rest of the ventricles becomes excitable again (18). Therefore, a larger excitable gap, as was observed in the area of the infarction in this study, can compromise shock outcome. In this study, an image-based cardiac model with unprecedented structural detail has been used for the first time to demonstrate the formation of VEPs.

### *B. Reentry in the right-ventricular free wall*

A geometrical mesh of the right-ventricular (RV) free wall was extracted from the model of the normal rabbit heart shown in Figure 4. Figure 9A illustrates the extracted RV wall. Since DTMR data were not available for the normal rabbit case, fiber orientations were assigned to the elements using a recently developed algorithm (25). This algorithm has been found to match DTMR-derived fiber orientations with

an accuracy of 95%. The resultant RV free wall model consisted of approximately 15 million elements.

The tissue active response was modeled again using the rabbit ventricular ionic model (19). Pacing stimuli were applied from the apex (bottom of Figure 9B-F), beginning at a basic cycle length of 210 ms and decreasing to a minimum of 168 ms. After eight pulses were applied at a cycle length of 168 ms, a large stimulus was applied to the lower right quarter of the model in the refractory tail of the last paced wave. This initiated one beat of re-entry (ending as shown in Figure 9B). Three line stimuli were applied in the excitable gap of this re-entrant wave (as shown in Figure 9C-D) in order to re-initiate reentry until the tissue was able to sustain a re-entrant wave unassisted. In Figure 9D the voltage map was taken at time of stimulus application, while the activation map shows from then through 60 ms later. Colored isochrones in Figure 9C represent 10 ms of propagation per color as shown in the scale. An example of one beat of such reentry is shown in Figure 9E-F. In Figure 9F, voltage map was taken in the middle of the period shown in Figure 9E. The Black arrow in Figure 9E indicates approximate direction of propagation starting at the circle and ending near the arrow. Colored isochrones in Figure 9E represent 10 ms of propagation per color, with values indicated by the scale. The reentrant pathway is shown in Figure 9E, while a snapshot of transmembrane potential during the same reentrant beat is shown in Figure 9F. Re-entry was sustained for at least three seconds.

During reentry, no consistent reentrant pathway was observed. Rather, on each rotation the wave meandered through the various endocardial structures and the bulk tissue in the ventricular wall. The long, thin network of strands was occasionally responsible for transmitting activation to a region at rest, although typically the activation wavefront moved through the bulk of the wall itself. Qualitatively, the pattern of wavefront propagation was reminiscent of polymorphic rather than monomorphic ventricular tachycardia. The simulation study enables us for the first time to examine the role of endocardial structures such as trabeculations in initiation and maintenance of reentry.

## VI. CONCLUDING REMARKS

This report presents a set of generic methods for reconstructing high-resolution 3D heart models from structural MR and DTMR images, and demonstrates the utility of these models in the study of arrhythmia and defibrillation. The models presented in this paper offer hitherto unavailable structural detail, heralding enhanced opportunities for modeling cardiac electrophysiology. In particular, our models contain fine details of the cardiac geometry such as endocardial trabeculations and the Purkinje system, and incorporate atrial and ventricular fiber data acquired at resolutions in the order of  $10^{-4}$  m. The simulation studies presented here are the first to demonstrate that highly detailed image-based cardiac models can be used in the study of arrhythmia and defibrillation.

## REFERENCES

- [1] P. J. Hunter, A. J. Pullan, and B. H. Smaill. Modeling Total Heart Function. *Annual review of biomedical engineering* 2003; 5: 147.
- [2] R. A. B. Burton, G. Plank, J. E. Schneider, V. Grau, H. Ahammer, S. L. Keeling, J. Lee, N. P. Smith, D. Gavaghan, N. Trayanova, and P. Kohl. Three-Dimensional Models of Individual Cardiac Histoanatomy: Tools and Challenges. *Annals of the New York Academy of Sciences* 2006; 1080: 301.
- [3] P. A. Helm, L. Younes, M. F. Beg, D. B. Ennis, C. Leclercq, O. P. Faris, E. McVeigh, D. Kass, M. I. Miller, and R. L. Winslow. Evidence of Structural Remodeling in the Dyssynchronous Failing Heart. *Circulation Research* 2006; 98: 125.
- [4] J. S. Suri, S. S. Kamaledin, and S. Singh: *Advanced Algorithmic Approaches to Medical Image Segmentation: State of the Art Applications in Cardiology, Neurology, Mammography, and Pathology*, London, Springer-Verlag, 2002.
- [5] L. Ibanez, W. Schroeder, L. Ng, and J. Cates: *The Itk Software Guide: The Insight Segmentation and Registration Toolkit*, Kitware Inc, 2003.
- [6] J. Chen, W. Liu, H. Zhang, L. Lacy, X. Yang, S.-K. Song, S. A. Wickline, and X. Yu. Regional Ventricular Wall Thickening Reflects Changes in Cardiac Fiber and Sheet Structure During Contraction: Quantification with Diffusion Tensor MRI. *American Journal of Physiology - Heart and Circulatory Physiology* 2005; 289: H1898.
- [7] P. J. Basser and C. Pierpaoli. Microstructural and Physiological Features of Tissues Elucidated by Quantitative-Diffusion-Tensor MRI. *Journal of Magnetic Resonance* 1996; 111: 209.
- [8] J. Chen, S.-K. Song, W. Liu, M. McLean, S. J. Allen, J. Tan, S. A. Wickline, and X. Yu. Remodeling of Cardiac Fiber Structure after Infarction in Rats Quantified with Diffusion Tensor MRI. *American Journal of Physiology - Heart and Circulatory Physiology* 2003; 285: H946.
- [9] A. Schmidt, C. F. Azevedo, A. Cheng, S. N. Gupta, D. A. Bluemke, T. K. Foo, G. Gerstenblith, R. G. Weiss, E. Marbán, G. F. Tomaselli, J. A. C. Lima, and K. C. Wu. Infarct Tissue Heterogeneity by Magnetic Resonance Imaging Identifies Enhanced Cardiac Arrhythmia Susceptibility in Patients with Left Ventricular Dysfunction. *Circulation* 2007; 115: 2006.
- [10] M.-T. Wu, W.-Y. I. Tseng, M.-Y. M. Su, C.-P. Liu, K.-R. Chiou, V. J. Wedeen, T. G. Reese, and C.-F. Yang. Diffusion Tensor Magnetic Resonance Imaging Mapping the Fiber Architecture Remodeling in Human Myocardium after Infarction: Correlation with Viability and Wall Motion. *Circulation* 2006; 114: 1036.
- [11] A. J. Prassl, F. Kickinger, H. Ahammer, V. Grau, J. E. Schneider, E. Hofer, E. J. Vigmond, N. A. Trayanova, and G. Plank. Automatically Generated, Anatomically Accurate Meshes for Cardiac Electrophysiology Problems. *IEEE Transactions on Biomedical Engineering* 2008; in revision.
- [12] S. C. Kim, A. VasANJI, I. Efimov, and Y. Cheng. Spatial Distribution and Extent of Electroporation by Strong Internal Shock in Intact Structurally Normal and Chronically Infarcted Rabbit Hearts. *Journal of*

- Cardiovascular Electrophysiology 2008; in press.
- [13] F. Vadakkumpadan, H. Arevalo, A. J. Prassl, J. Chen, F. Kickinger, P. Kohl, G. Plank, and N. Trayanova. Image-Based Models of Cardiac Structure in Health and Disease. *IEEE Transactions on Medical Imaging* 2008; under review.
  - [14] D. Rohmer, A. Sitek, and G. T. Gullberg. Reconstruction and Visualization of Fiber and Laminar Structure in the Normal Human Heart from Ex Vivo Diffusion Tensor Magnetic Resonance Imaging (DTMRI) Data. *Investigative Radiology* 2007; 42: 777.
  - [15] P. Perona and J. Malik. Scale-Space and Edge Detection Using Anisotropic Diffusion. *IEEE Transactions on Pattern Analysis and Machine Intelligence* 1990; 12: 629.
  - [16] P. Helm, M. F. Beg, M. Miller, and R. Winslow. Measuring and Mapping Cardiac Fiber and Laminar Architecture Using Diffusion Tensor MR Imaging. *Annals of the New York Academy of Sciences* 2005; 1047: 296.
  - [17] D. D. J. Streeter, H. M. Spotnitz, D. P. Patel, J. J. Ross, and E. H. Sonnenblick. Fiber Orientation in the Canine Left Ventricle During Diastole and Systole. *Circulation Research* 1969; 24: 339.
  - [18] N. Trayanova. Defibrillation of the Heart: Insights into Mechanisms from Modelling Studies. *Experimental Physiology* 2006; 91: 323.
  - [19] A. Mahajan, Y. Shiferaw, D. Sato, A. Baher, R. Olcese, and L. H. Xie. A Rabbit Ventricular Action Potential Model Replicating Cardiac Dynamics at Rapid Heart Rates. *Journal of Biophysics* 2008; 94: 392.
  - [20] Y. Cheng, K. Mowrey, D. V. Wagoner, P. J. Tchou, and I. R. Efimov. Virtual Electrode-Induced Reexcitation: A Mechanism of Defibrillation. *Circulation Research* 1999; 85: 1056.
  - [21] K. Skouibine, N. Trayanova, and P. Moore. A Numerically Efficient Model for Simulation of Defibrillation in an Active Bidomain Sheet of Myocardium. *Mathematical Biosciences* 2000; 166: 85.
  - [22] V. Jacquemet and C. S. Henriquez. Modelling Cardiac Fibroblasts: Interactions with Myocytes and Their Impact on Impulse Propagation. *Europace* 2007; 9: 29.
  - [23] B. J. Roth. Electrical Conductivity Values Used with the Bidomain Model of Cardiac Tissue. *IEEE Transactions on Biomedical Engineering* 1997; 44: 326.
  - [24] N. L. Walker, F. L. Burton, S. Kettlewell, G. L. Smith, and S. M. Cobbe. Mapping of Epicardial Activation in a Rabbit Model of Chronic Myocardial Infarction. *Journal of Cardiovascular Electrophysiology* 2007; 18: 862.
  - [25] J. D. Bayer, G. Plank, A. J. Prassl, and N. A. Trayanova. Assigning Fiber and Sheet Orientations to Unstructured Meshes of Cardiac Tissue: A Novel Rule-Based Approach. 2008; in preparation.

## FIGURE CAPTIONS

Figure 1. The application of the segmentation pipeline to an example image slice. The sequence of rectangular blocks illustrate the results as an example image slice is processed through the steps 1 to 4 in the pipeline.

Figure 2. Mesh generation: (a) mesh corresponding to the segmented image slice shown in Figure 1; (b) enlarged view of the small region enclosed by the magenta box in (a).

Figure 3. Assignment of fiber orientations: (a) 2D projection of orientations assigned to the mesh shown in Figure 2a; (b) enlarged view of the small region enclosed by the magenta box in (a).

Figure 4. The models of normal and infarcted rabbit hearts. In each row, the first column shows the anterior view of the entire model, and the second and third columns show the model split in half along a horizontal long axis view plane.

Figure 5. Demonstration of the structural detail that can be obtained using our processing pipeline: (a) the endocardial trabeculations in the basal region of the right ventricle in the normal rabbit model; (b) a papillary muscle that is attached to the mitral valve of the infarcted rabbit model; (c) blood vessels and interlamina clefts in the normal rabbit model

Figure 6. Visualization of fiber tracks, indicative of regionally prevailing cell orientation, in the infarcted rabbit model. (a) epicardial view of tracks in the entire model; (b) tracks in a slab of tissue between two short axis planes.

Figure 7. Reconstructing the Purkinje system: (A) a slab of the mesh that lies between two short axis

planes; (B) the PMJs, PPJs, and tags on a short axis slice of the image. The inset displays the enlarged view of the small region enclosed in the red box; (C) the reconstructed Purkinje system; (D) the Purkinje system overlaid on the mesh.

Figure 8. Simulations of the infarcted rabbit model showing the effect of the infarct core on shock-end virtual electrode polarizations. (a) The whole heart model with infarct core (blue), border zone (green), and the plate electrodes; (b) The heart cut in half at a coronal plane (c) Transmembrane potential at shock-end of a 1 V/cm left ventricular shock; (d) Transmembrane potential at shock-end of a 5 V/cm left ventricular shock; (e) Transmembrane potential at shock-end of a 1 V/cm right ventricular shock; (f) Transmembrane potential at shock-end of a 5 V/cm right ventricular shock. The color bar for (c) through (f) is shown in the bottom panel. Transmembrane potentials  $\leq -90$  mV are colored as  $-90$  mV, and potentials  $\geq 20$  mV are colored as  $20$  mV.

Figure 9. Initiation of an apical wave reentry in the rabbit right ventricular free wall. (A) surface of rabbit ventricles with right-ventricular wall boxed in; (B) voltage map of second re-entrant beat initiated by premature line stimulus in the wake of a propagating wave; (C, D) activation and voltage maps (respectively) of third and final pacing stimulus and subsequent wave propagation; (E, F) activation and voltage maps (respectively) of a reentrant beat following initiation as shown in C and D. The color bar in B applies to D and F also.

FIGURES

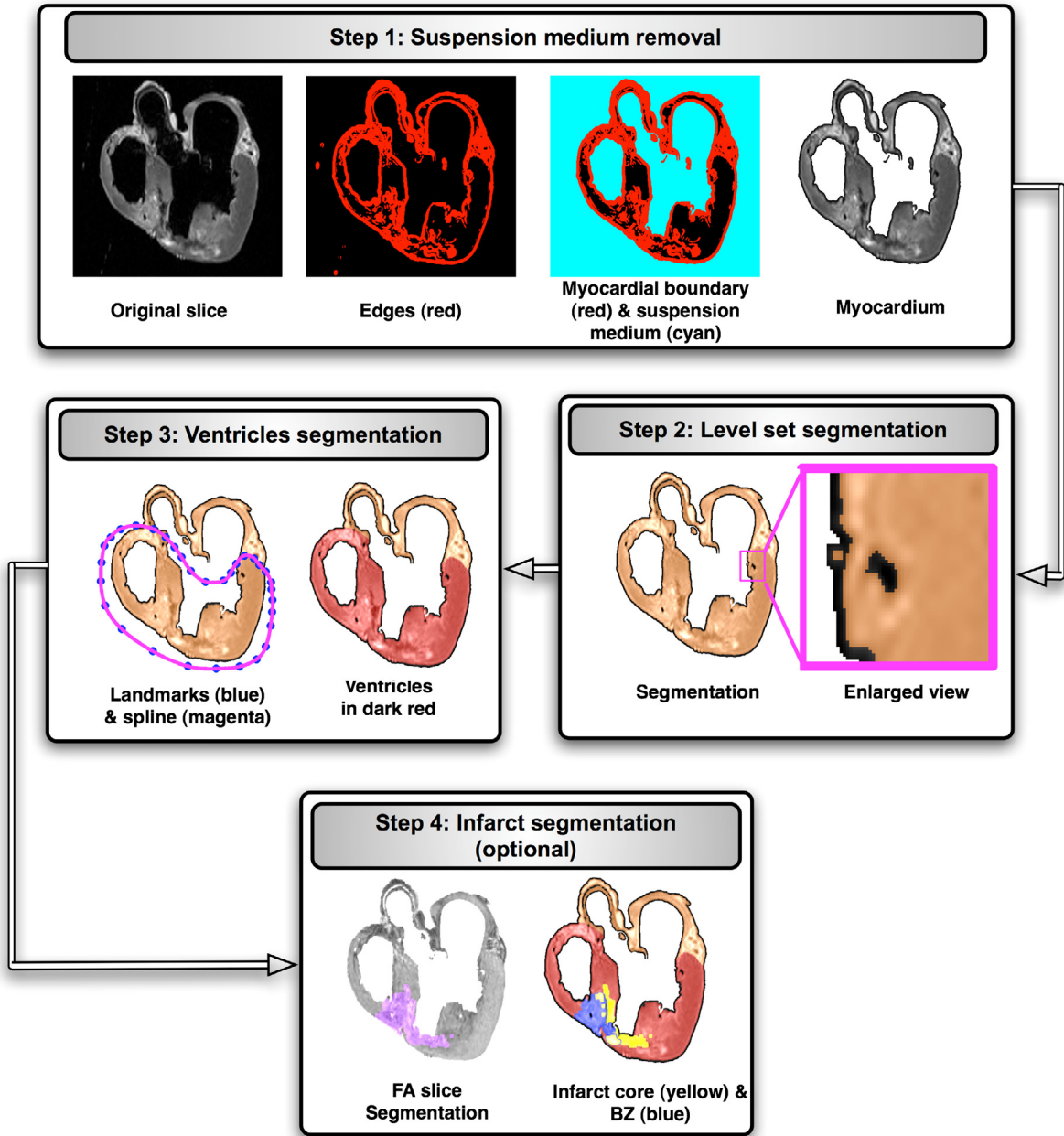
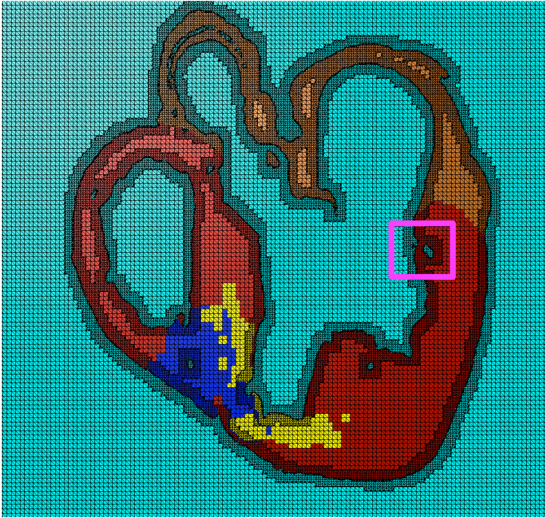
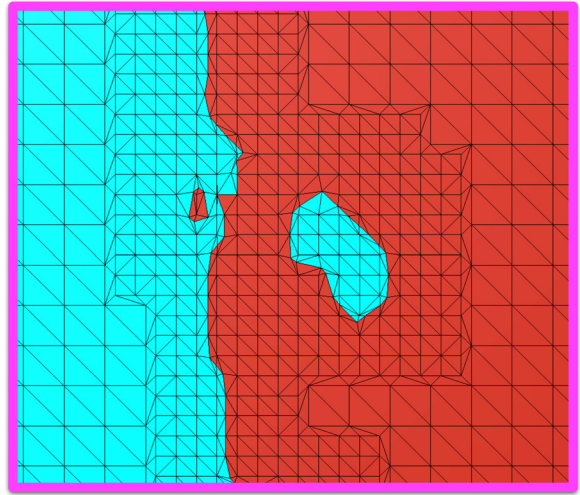


Figure 1.



(a)



(b)

Figure 2.

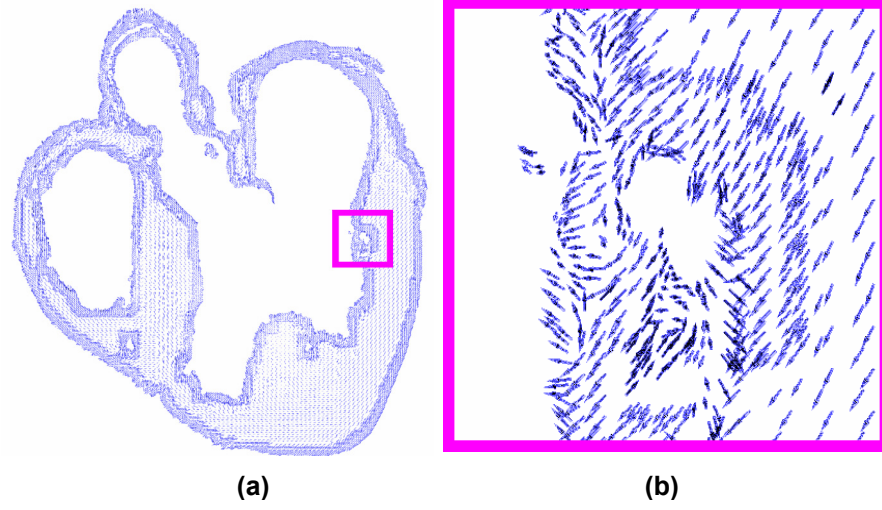


Figure 3.

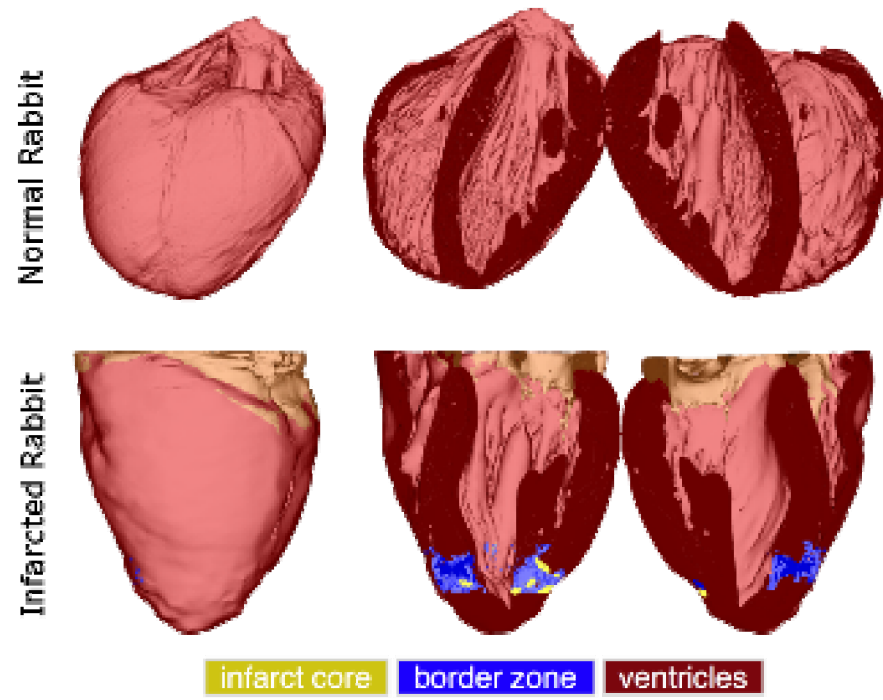


Figure 4.

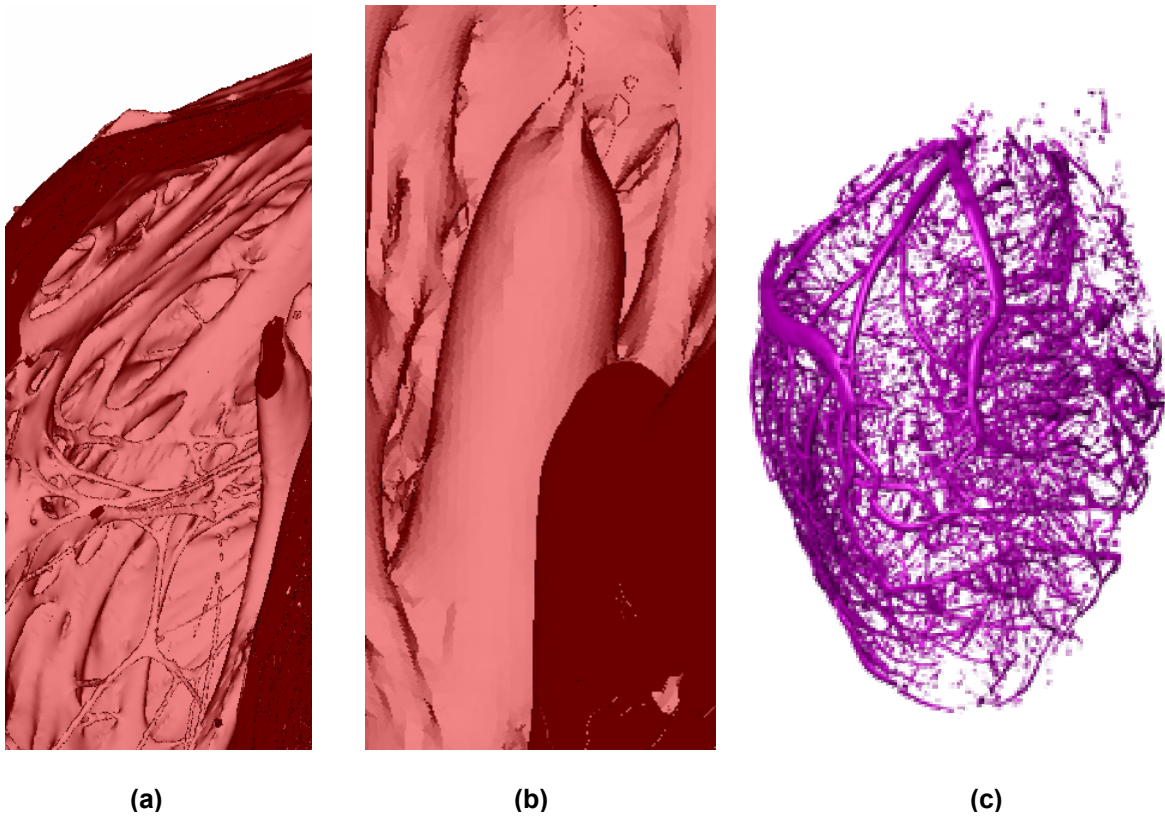
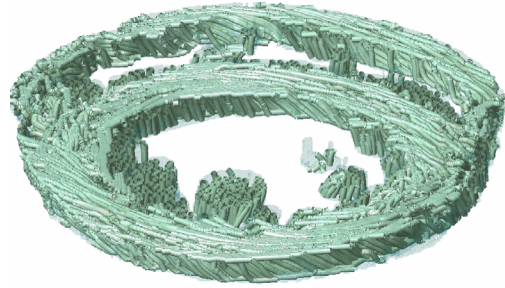


Figure 5.



**(a)**



**(b)**

Figure 6.

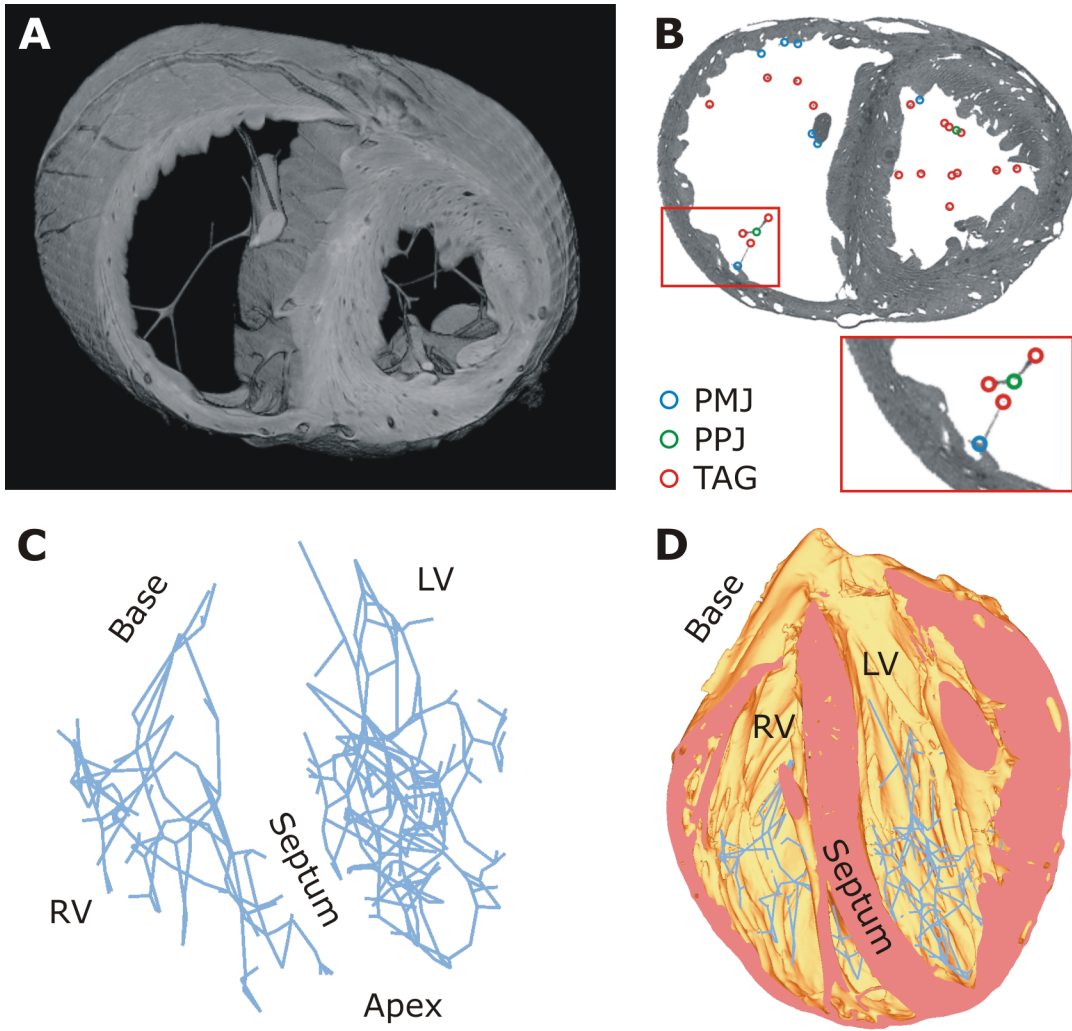


Figure 7.

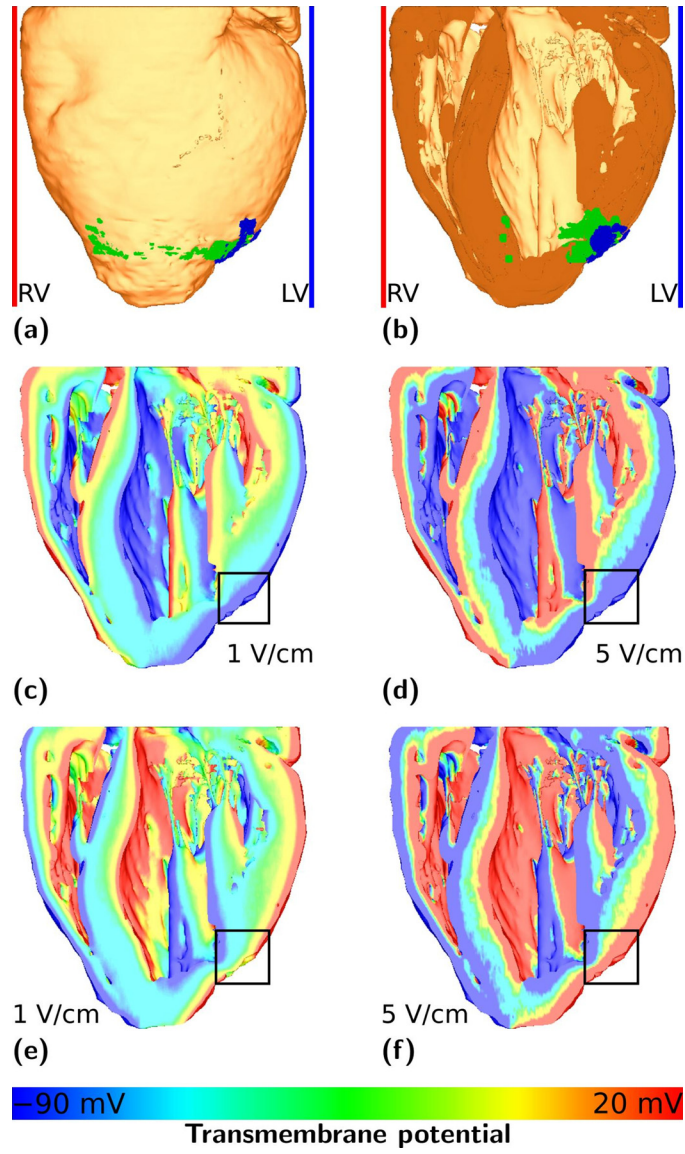


Figure 8.

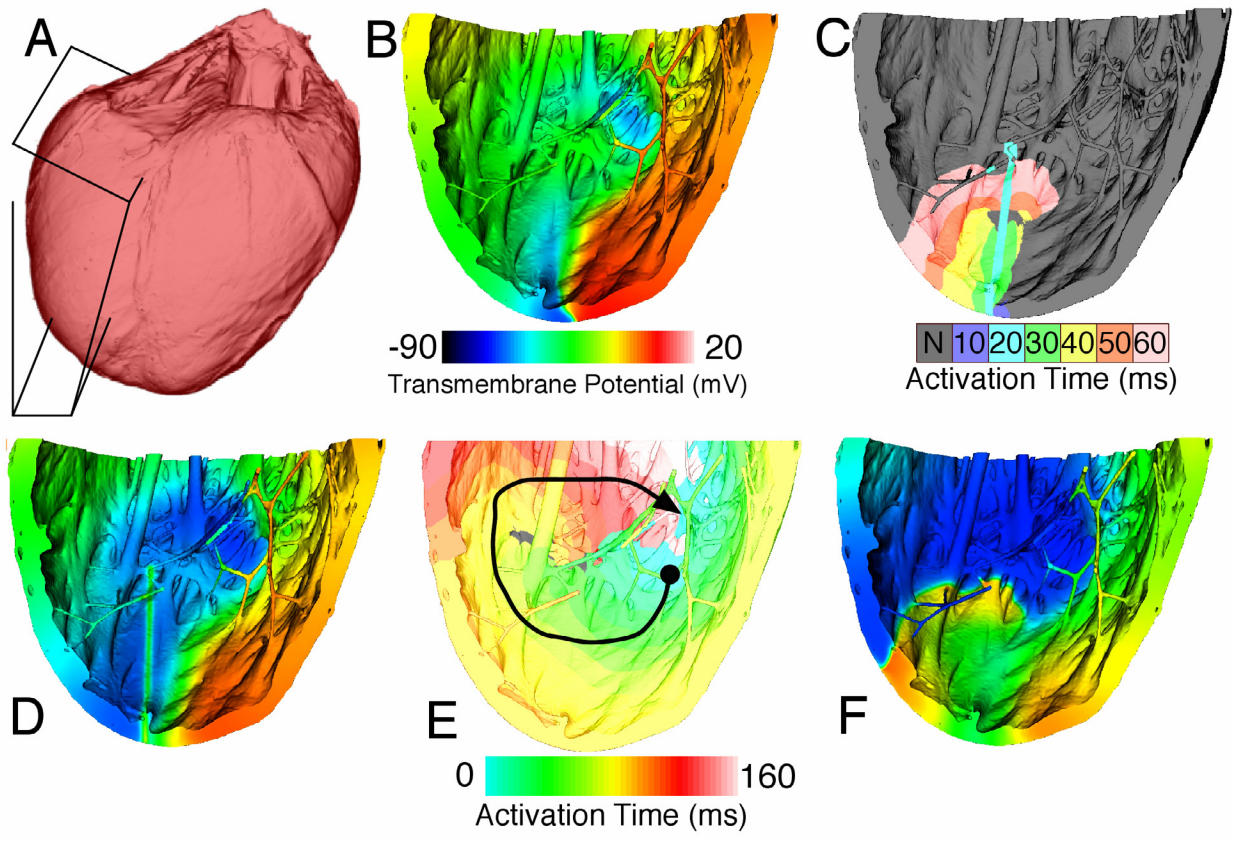


Figure 9.